Bull Volcanol
DOI 10.1007/s00445-011-0483-y

RESEARCH ARTICLE

Spatio-temporal evolution of Yellowstone deformation between 1992 and 2009 from InSAR and GPS observations

Mohamed H. Aly · Elizabeth S. Cochran

Received: 26 May 2010 / Accepted: 31 March 2011

Abstract In this study, the spatio-temporal evolution of Yellowstone deformation between 1992 and 2009 is monitored using interferometric synthetic aperture radar (InSAR) data acquired by the European Remote-Sensing Satellites (ERS-1 and ERS-2) and the Environmental Satellite (ENVISAT). These data are combined with continuous global positioning system (GPS) measurements to identify four discrete episodes of caldera subsidence and uplift, these episodes are: 1992–1995 (subsidence of 2.7 cm/year), 1996–2000 (subsidence of 0.5 cm/year, with local uplift of 1.7 cm/year at Norris), 2000–2004 (subsidence of 0.7 cm/year, with local uplift of 0.6 cm/year at Norris), and 2004–2009 (uplift of 3–8 cm/year, with local subsidence of 1–4 cm/year at Norris). We construct the full three-dimensional velocity field of Yellowstone deformation for 2005–2006 from ascending and descending ENVISAT orbits. The InSAR three-dimensional velocity field and three-component GPS measurements indicate that the majority of the observed deformation (3–8 cm/year) across the Yellowstone caldera and near Norris Geyser Basin (NGB) occurred in the vertical direction between the summers of 2005 and 2006. During this time, significant lateral displacements of 3–7 cm/year also occurred in the east–west direction at the southeastern and western rims of the Yellowstone caldera and in the area between Hebgen Lake and NGB. Minor north–south displacements of about 0.2 cm/year also occurred, however, in the southwestern section of the caldera and near Yellowstone Lake during the same period. The calculated three-dimensional velocity field for 2005–2006 implies the existence of two pressure-point sources, beneath the two structural resurgent domes in the Yellowstone caldera, connected by a planar conduit, rather than a single, large sill as proposed in previous studies. Furthermore, no measurable displacements occurred along any fault zone across the caldera during the entire period of observation (1992–2009). Therefore, we infer that magmatic and hydrothermal processes beneath the Yellowstone caldera and NGB were the main sources of deformation.

Keywords Yellowstone caldera · Radar interferometry · Three-dimensional velocity · Volcanic deformation · Kinematic and geodetic modeling

Editorial responsibility: A. Harris

M. H. Aly (✉) · E. S. Cochran
Department of Earth Sciences, University of California-Riverside, Riverside, CA 92521-0423, USA
e-mail: drmaly@ucr.edu

Introduction

The Yellowstone Plateau (Fig. 1) is one of the most concentrated regions of magmatic, hydrothermal, and seismic activity in North America (e.g., Pelton and Smith 1979; Dzurisin and Yamashita 1987; Dzurisin et al. 1990, 1994; Christiansen 2001; Waite and Smith 2002; Wicks et al. 2006; Vasco et al. 2007; Aly et al. 2009). It is thus a critical region in which regular monitoring is required to track the evolution of potentially hazardous events that may affect millions of people.

The Yellowstone Plateau volcanic field was formed during three major caldera-forming eruptions that occurred at approximately 2.05, 1.3, and 0.64 Ma (Christiansen 2001). The most recent eruption formed the current Yellowstone caldera (Christiansen 2001) as shown in Fig. 1. Approximately 50 rhyolitic and basaltic events occurred since this last cataclysmic eruption in association with the development of Yellowstone caldera, with the

Published online: 01 June 2011

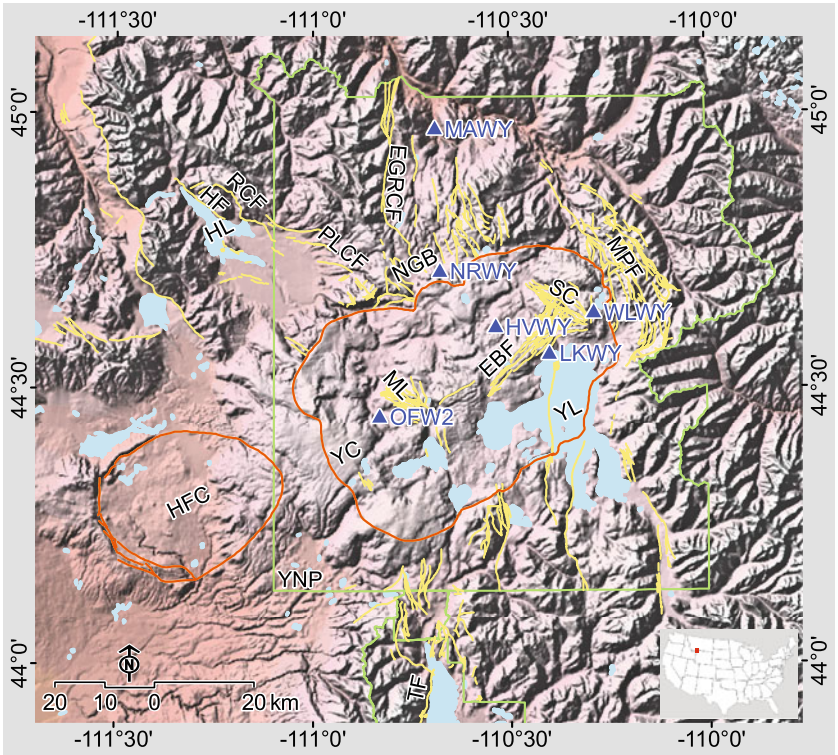

Fig. 1 Hill-shaded relief of the greater Yellowstone region. The *light blue areas* are water bodies and the *yellow lines* mark the Quaternary faults (U.S. Geological Survey 2006). *Orange* represents topographic margins of the Yellowstone caldera and the Henrys Fork caldera, and *green* represents the boundary of Yellowstone National Park. *HF* indicates Hebgen fault, *RCF* Red Canyon fault, *PLCF* Post-Lava Creek fault, *ESRCF* East Gallatin-Reese Creek fault, *MPF* Mirror Plateau fault, *EBF* Elephant Back fault, *TF* Teton fault, *HL* Hebgen Lake, *YL* Yellowstone Lake, *YC* Yellowstone caldera, *SC* Sour Creek resurgent dome, *ML* Mallard Lake resurgent dome, *HFC* Henrys Fork caldera, *NGB* Norris Geyser Basin, *YNP* Yellowstone National Park. The *small blue triangles* indicate the locations of continuous GPS stations (OFW2, WLWY, HVWY, NRWY, LKWY, and MAWY)

youngest events occurring at around 70 ka (Christiansen et al. 2007). Although no eruptions occurred since 70 ka, the Yellowstone volcanic system is still active as indicated by its alternating decadal episodes of subsidence and uplift, widespread hydrothermal activity, and extensive seismicity (e.g., Pelton and Smith 1979; Dzurisin and Yamashita 1987; Dzurisin et al. 1990, 1994; Waite and Smith 2002; Wicks et al. 1998, 2006).

Long-term geodetic monitoring indicates that the Yellowstone caldera is in a virtually constant state of unrest (Vasco et al. 2007). Geodetic measurements reveal multiple cycles of inflation and deflation between 1923 and 2004, with maximum average rates of 1–2 cm/year across the caldera and near Norris Geyser Basin (NGB) (Pelton and Smith 1979, 1982; Dzurisin et al. 1990, 1994). The observed inflation cycles are attributed to repeated intrusions of magma into the upper crust beneath the caldera or to pressurization of the hydrothermal system by fluids released from a deep crystallizing body of rhyolitic magma beneath the caldera (e.g., Dzurisin et al. 1994; Waite and Smith 2002; Wicks et al. 2006). Analogous to Yellowstone, results from Rinaldi et al. (2010) show that extensive degassing of a magmatic source beneath the Campi Flegrei caldera in Italy may cause several centimeters of ground uplift. Conversely, the episodes of Yellowstone deflation are explained by magma migration from beneath the caldera or depressurization, and fluid loss, from the deep hydrothermal system (e.g., Dzurisin et al. 1990; Waite and Smith 2002; Vasco et al. 2007). Sagging of the caldera floor in response to regional crustal extension is considered also as a source of subsidence across the Yellowstone caldera (Dzurisin et al. 1994). Although Hurwitz et al. (2007) and Peltier et al. (2009) proposed models that could explain the inflation of large calderas solely by pressurization of the hydrothermal system, we believe that combinations of two or more of the aforementioned processes most likely drive the deformation at Yellowstone. Similar inferences were made by Gottsmann et al. (2006) to explain the inflation and deflation occurred between 1981 and 2001 at Campi Flegrei.

In July 2004, the Yellowstone caldera began a new cycle of inflation that progressed at a rate of about 7 cm/year during 2004–2006 (Chang et al. 2007). This rate is more than three times faster than historical inflation rates, as revealed by the global positioning system (GPS) and synthetic aperture radar interferometry (InSAR) measurements of Chang et al. (2007). Other previous studies also employed InSAR and/or GPS to track the Yellowstone deformation over short time periods, including 1992–1997 (Wicks et al. 1998; Dzurisin et al. 1999), 1996–2003 (Wicks et al. 2006), and 1992–2002 (Vasco et al. 2007).

In this study, we provide a complete series of differential InSAR interferograms spanning 1992–2009, supported by GPS measurements from six continuous stations located in Fig. 1, to comprehensively monitor and investigate the spatio-temporal evolution of Yellowstone deformation. We present new interferograms spanning 2000–2004, 2004–

2008, and 2008–2009 and provide a full three-dimensional velocity field constructed from ascending and descending ENVISAT orbits for the Yellowstone caldera and its surroundings. The results provide new insights into the shape of the magma chamber beneath the Yellowstone caldera and allow us to develop a new conceptual model for the Yellowstone volcanic system.

InSAR data processing

Creation of the differential interferograms

The InSAR scenes used in this study were acquired by the European Remote-Sensing Satellites (ERS-1 and ERS-2) between 1992 and 2004 and the Environmental Satellite (ENVISAT) between 2004 and 2009. Detailed information of the used scenes is provided in Table 1. The two-pass interferometric approach (e.g., Gabriel et al. 1989) is employed to create differential interferograms by first constructing the phase difference between InSAR pairs and then removing the topographic signature using a digital elevation model (DEM) with a 1-arc sec spatial resolution, produced from the Shuttle Radar Topography Mission (SRTM). The precise orbital information provided by the European Space Agency is used to compensate for orbital errors, and later the corrected interferograms are unwrapped to convert the cyclic phase values to continuous values.

Although 24 interferograms are created, nine are used to summarize the deformation that occurred at Yellowstone between 1992 and 2009. The selected interferograms span time periods with similar directions, spatial extents, and rates of deformation as determined by examining the full time series and previous InSAR results (e.g., Wicks et al. 1998, 2006; Vasco et al. 2007), as well as geodetic measurements from continuous GPS stations. This examination shows that the deformation rate was slow and the deformation vectors were nearly constant between 1992 and 1995. Therefore, the two ERS interferograms spanning 1992–1993 and 1993–1995 are stacked to present the cumulative deformation for the 1992–1995 period.

Atmospheric artifacts are always potential sources of errors in InSAR measurements and can introduce phase disturbances with standard deviations of 0.5 cm (e.g., Hoffmann et al. 2003). They have a low spatial frequency and tend to be temporally uncorrelated (e.g., Zebker et al. 1997). Therefore, a pair-wise comparison following the method of Massonnet and Feigl (1995) is employed to assess the presence of atmospheric artifacts in the processed interferograms; interferograms that are extensively contaminated by atmospheric effects are discarded.

Topographic uncertainties in the DEM used to remove the topographic contribution from the interferograms are also a potential source of error. However, we used only InSAR pairs of short perpendicular baselines (45–243 m), thus our interferograms are relatively insensitive to errors in the SRTM DEM. Moreover, where our InSAR measurements overlap with previous InSAR and GPS measurements, the observed deformation patterns and magnitudes are consistent. The corrected differential interferograms are presented in Fig. 2, and two displacement profiles across each interferogram are given in Fig. 3.

Calculation of the three-dimensional velocity field

A critical limitation of InSAR measurements is that an interferogram depicts only one component of surface deformation in the radar line-of-sight. However, it is possible to resolve the vertical and lateral components of crustal movements using data acquired from both ascending and descending orbits because the radar data are acquired by side-looking sensors with different imaging geometries.

Table 1 Raw InSAR data used in the investigation

Reference image			Slave image			$B_\perp$ (m)	Track/frame
Orbit	Satellite	Acquisition date (day/month/year)	Orbit	Satellite	Acquisition date (day/month/year)		
10206	ERS-1	28/06/1993	05697	ERS-1	17/08/1992	045	041/2709
21572	ERS-1	30/08/1995	10206	ERS-1	28/06/1993	177	041/2709
28452	ERS-2	28/09/2000	07410	ERS-2	19/09/1996	047	041/2709
48492	ERS-2	29/07/2004	27450	ERS-2	20/07/2000	091	041/2709
22919	ENVISAT	19/07/2006	13400	ENVISAT	22/09/2004	243	320/0891
22418	ENVISAT	14/06/2006	16907	ENVISAT	25/05/2005	103	320/0891
23141	ENVISAT	03/08/2006	17630	ENVISAT	14/07/2005	125	041/2709
32939	ENVISAT	18/06/2008	23420	ENVISAT	23/08/2006	097	320/0891
38450	ENVISAT	08/07/2009	33941	ENVISAT	27/08/2008	230	320/0891

$B_\perp$ the perpendicular baseline

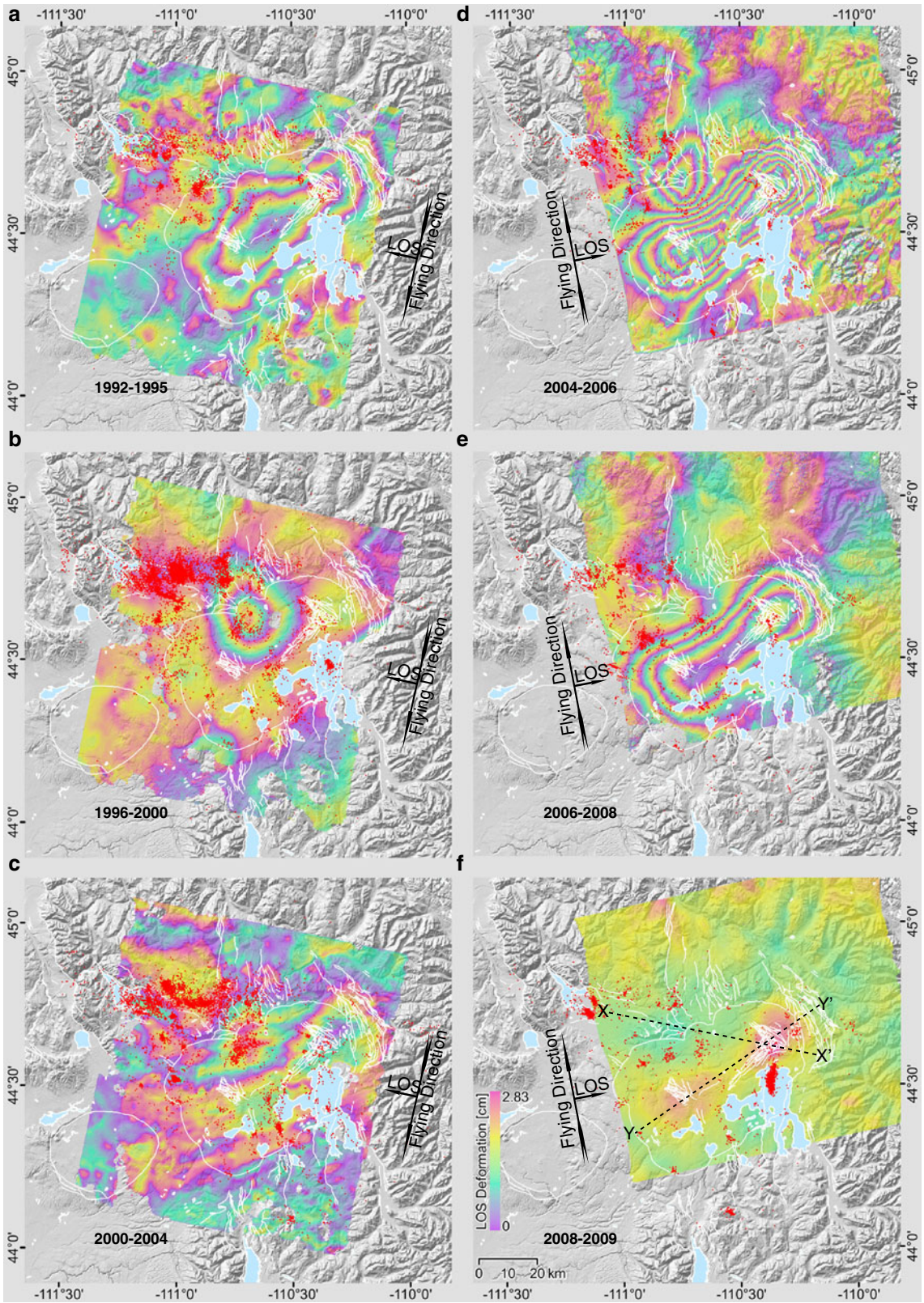

Here, we employ a similar approach to that of Fialko et al. (2001b) to calculate the three-dimensional velocity field using data from both ascending and descending ENVISAT advanced synthetic aperture radar orbits, but we do not use the azimuth offsets. Although azimuth offsets can be calculated by cross-correlation of two amplitude images,

◀ **Fig. 2** Line-of-sight deformation superimposed on the hill-shaded relief of the region. *Solid white lines* mark the Quaternary faults (U.S. Geological Survey 2006), *small red dots* indicate seismicity during each interferogram period (the earthquake records are from the University of Utah Seismographic Stations' Yellowstone National Park Earthquake Catalogs for 1983–2010), and *light blue areas* are water bodies. **a** ERS stacked interferogram of 17/08/1992–28/06/1993 and 28/06/1993–30/08/1995, **b** ERS interferogram of 19/09/1996–28/09/2000, **c** ERS interferogram of 20/07/2000–29/07/2004, **d** ENVISAT interferogram of 22/09/2004–19/07/2006, **e** ENVISAT interferogram of 23/08/2006–18/06/2008, and **f** ENVISAT interferogram of 27/08/2008–08/07/2009. The *dotted black lines* marked with *X-X′* and *Y-Y′* indicate the location of deformation profiles presented in Fig. 3

in the case of Yellowstone the signal-to-noise ratio is not sufficient for the azimuth offsets to be meaningful during 2005–2006, when interferogram pairs from ascending and descending ENVISAT orbits are available. The maximum lateral displacement calculated during this period is about 7 cm, but the accuracy of the interferogram azimuth offsets is supposed to be ~12.5 cm (assuming that we can calculate pixel offsets between the amplitude images to the accuracy of 1/32 pixel).

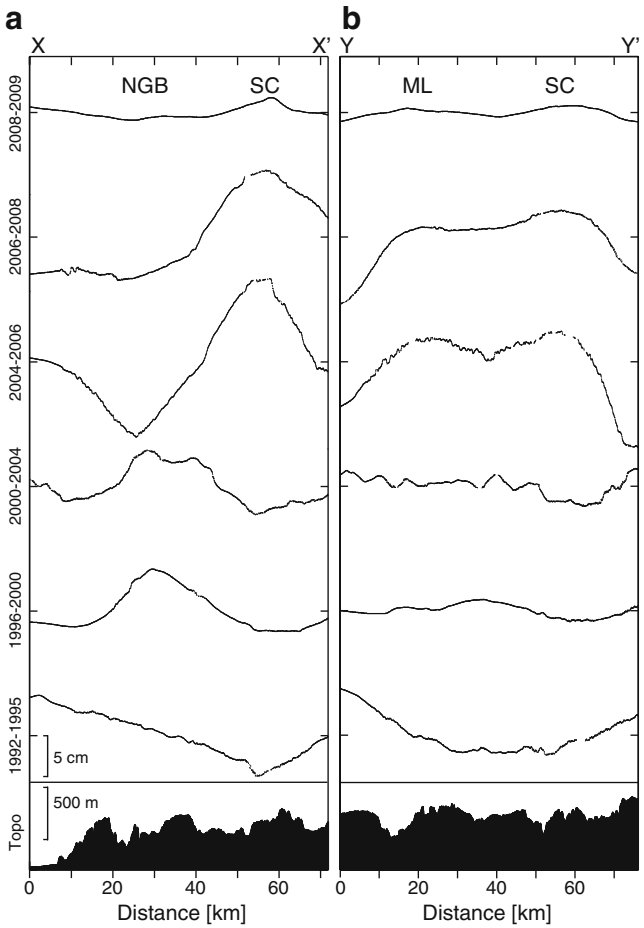

Fig. 3 Displacement profiles. **a** Profile X-X′ through all interferograms presented in Fig. 2 and **b** profile Y-Y′ through all interferograms presented in Fig. 2. Topography associated with the deformation profiles is shown in the bottom panels of (**a**) and (**b**)—note the topography scale starts at 2,000 m

We solve for the three orthogonal components of the surface velocity field from the two line-of-sight components by assuming that velocity vectors radiate from two central axes centered on the two structural domes in the Yellowstone caldera. Similar assumptions have been applied by Sandwell et al. (2002) and Yun et al. (2005) to resolve the vertical and lateral components of surface displacements. The line-of-sight vector, $\widehat{d}_{LOS}$, acquired in the right-looking direction can be expressed in terms of displacements as follows:

$$\left[\widehat{d}_{LOS}\right] = \begin{bmatrix} \hat{d}_v \\ \hat{d}_e \\ \hat{d}_n \end{bmatrix} [\cos\theta \; -\sin\theta\cos\phi \quad \sin\theta\sin\phi] \tag{1}$$

where $\hat{d}_v$, $\hat{d}_e$, and $\hat{d}_n$ are the vertical, easting, and northing displacement vectors, respectively; θ is the incidence angle (~23°); and ϕ is the azimuth of the ENVISAT heading vector (positive clockwise from north). The azimuth of the satellite-heading vector (ϕ) is −8.55° and 188.55° for ascending and descending orbits, respectively, as the orbit inclination (the angle between the heading vector of the ascending ENVISAT orbit and the easting vector at the equator) of the ENVISAT satellite is 98.55°. The derived three-dimensional velocity field is shown in Fig. 4.

The InSAR measurements are sensitive to surface displacements in the radar line-of-sight; this sensitivity decreases in all other directions because of the viewing geometry of the current radar sensors. As a result, vertical displacements can be measured using InSAR at a much better accuracy than lateral displacements. The northing displacement is always the least accurately resolved component due to lack of diversity in the viewing geometry of near-polar orbiting satellites such as ERS and ENVISAT. Wright et al. (2004) created several interferograms from images acquired from ascending and descending orbits with different look angles to improve the three-component calculations and assess the errors; unfortunately, only one pair of ENVISAT interferograms of the same look angle is available for the current study.

In contrast to sill-like bodies that produce little lateral displacements, equidimensional magma bodies produce more lateral displacements than vertical displacements (Fialko et al. 2001a; Segall 2010). Therefore, we can better deduce a range of non-unique shapes for the magma chamber beneath the Yellowstone caldera by measuring both lateral and vertical displacements. Two displacement profiles (Fig. 5) are created using the maximum vertical and easting components across the Sour Creek and Mallard

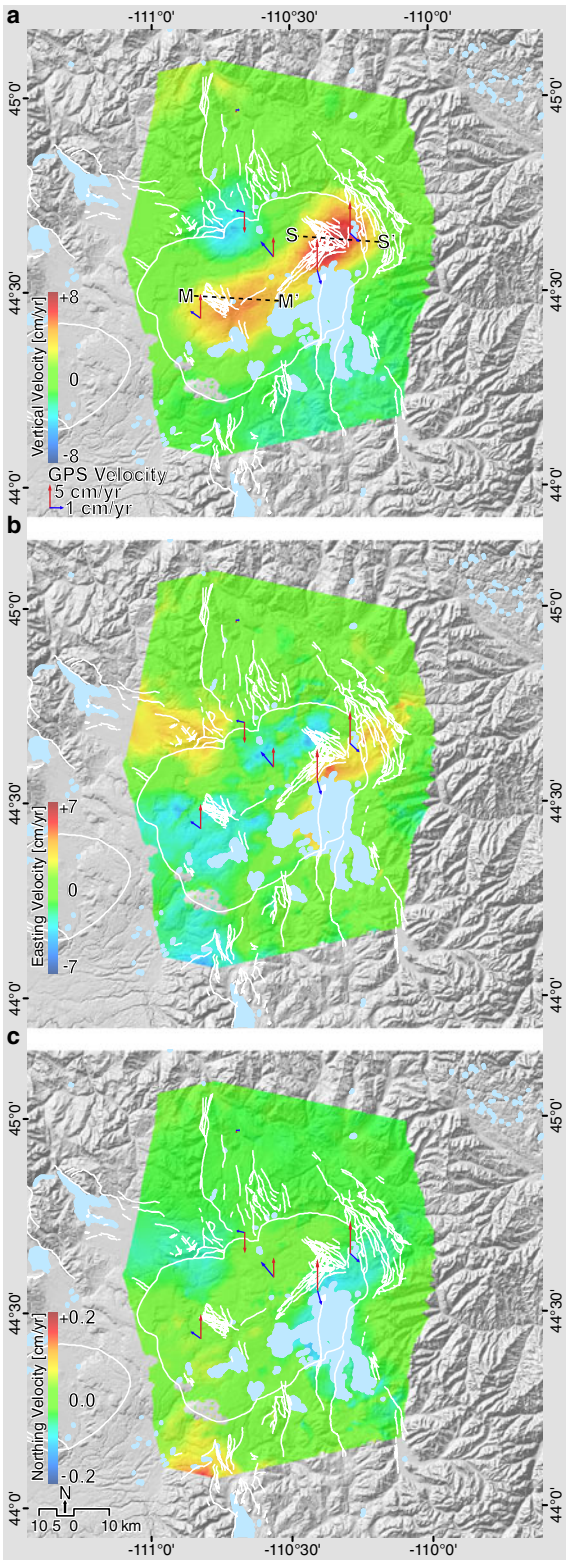

Fig. 4 InSAR three-dimensional velocity field of Yellowstone deformation between 2005 and 2006 assuming deformation results from two magma bodies underneath the Sour Creek and Mallard Lake resurgent domes. **a** Vertical velocity, **b** easting velocity, and (**c**) northing velocity. The S-S′ and M-M′ profiles are presented in Fig. 5a, b. The *red and blue arrows* indicate the vertical and horizontal GPS velocity vectors, respectively, during 2005–2006

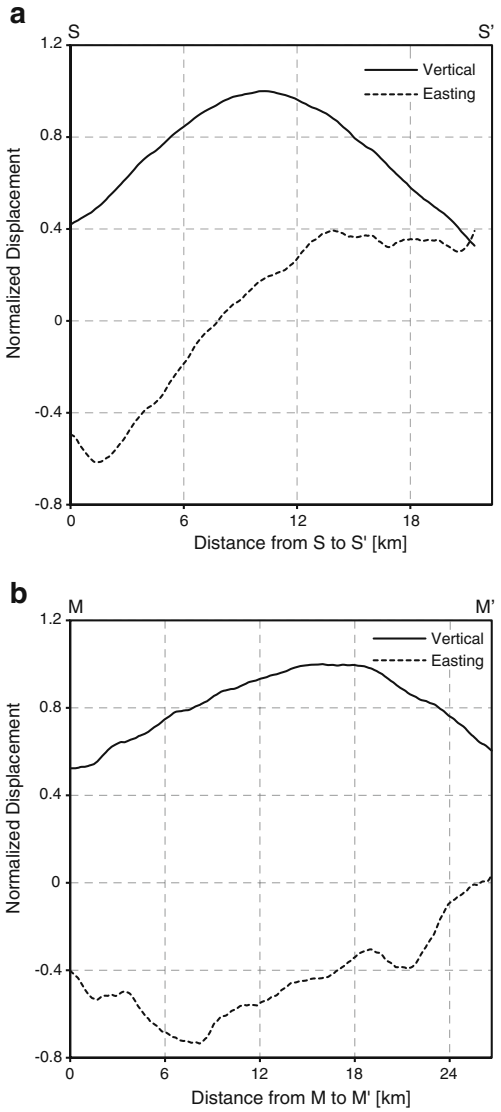

Fig. 5 Displacement profiles of the vertical and easting components. **a** Profile S-S′ across the Sour Creek resurgent dome and **b** profile M-M′ across the Mallard Lake resurgent dome. Values in both profiles are normalized by the maximum vertical displacement and three lines are averaged to smooth each profile. Locations of the S-S′ and M-M′ profiles are marked with dashed black lines in Fig. 4a

Lake resurgent domes, where large displacements are recorded. Then, the ratio of the maximum horizontal displacement to the maximum vertical displacement is calculated to determine the shape of magma chamber beneath the Yellowstone caldera.

GPS time-series analysis

To provide additional constraints on the timing of each episode of the Yellowstone deformation, we use Plate Boundary Observatory (PBO) GPS measurements from six continuous stations. Locations of the GPS stations are

shown in Fig. 1, where four stations (OFW2, WLWY, HVWY, and LKWY) are located inside the caldera and two stations (NRWY and MAWY) are located north of the caldera. Continuous GPS stations are separated by distances of ~12–50 km from each other. These stations were installed between 1996 and 2003 by the University of Utah (Puskas et al. 2007) and have been operated in collaboration with the EarthScope PBO since 2005. GPS data prior to 2004 from stations LKWY and MAWY are obtained from the Scripps Orbit and Permanent Array Center (SOPAC) (http://sopac.ucsd.edu/dataArchive).

Precise satellite orbits from the International Global Navigation Satellite System Service are used to solve for the daily coordinate solution, and station positions are calculated relative to the base sites located in the ITRF2000 reference frame (e.g., Hofmann-Wellenhof et al. 1992). The vertical, easting, and northing motions of each of the six stations are calculated with respect to the Stable North America Reference Frame (SNARF) using least squares estimations and are shown in Fig. 6. SNARF includes a network of GPS stations in the Rocky Mountain tectonic province and its adjacent areas to the east.

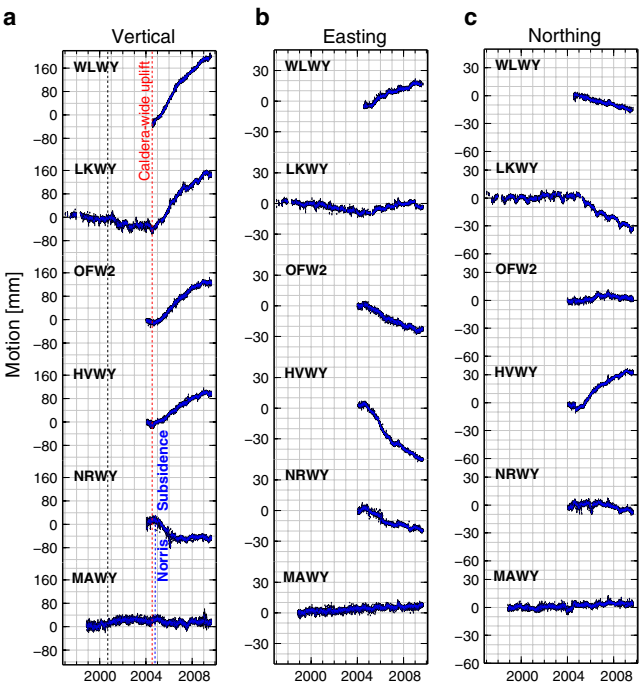

Fig. 6 GPS time series showing the three-component velocities of six continuous GPS stations (OFW2, WLWY, HVWY, NRWY, LKWY, and MAWY). Geographic locations of the GPS stations are marked with *small blue triangles* in Fig. 1. **a** Vertical motion, **b** easting motion, and **c** northing motion. This figure has been created using the Generic Mapping Tools (Wessel and Smith 1995)

Kinematic and geodetic modeling

We use a joint inversion of InSAR and GPS measurements to model ground displacements (Fig. 7) at Yellowstone. The interferogram of 2005–2006 is sub-sampled using quad-tree (e.g., Simons et al. 2002) to reduce the number of redundant points in the InSAR data, and a weighting scheme similar to that used by Fialko (2004) is applied to prevent the large number of InSAR data points from dominating the few GPS points in the model. However, because the GPS vertical components are redundant to and less accurate than the InSAR measurements, only the GPS horizontal components are included in the joint inversion. The sub-sampled InSAR points and GPS horizontal components are independent measurements, thus we apply the standard F tests of statistical significance to estimate the confidence intervals of the model parameters.

We model the deformation signals in an elastic, isotropic half-space with a Poisson's ratio of 0.25 and a rigidity of 30 GPa. The relationship between surface displacements and source parameters can be expressed as:

$$d = g(m) + e \tag{2}$$

where d is the observed surface displacement, m is the model source parameter, g is the Green's function that connects d to m, and e is the observation error.

The best-fitting source geometry that minimizes the differences between the geodetic measurements and model predictions is calculated using a nonlinear optimization method (Monte-Carlo inversion) and the point source strengths are calculated using a linear inversion. Our model includes three pressure-point sources (Mogi 1958) beneath the two resurgent domes and NGB, plus a rectangular dislocation source (Okada 1985, 1992) that connects the two Mogi sources beneath the resurgent domes (Fig. 7). Four parameters are specified for each point source: longitude, latitude, centroid depth, and strength and eight parameters for the dislocation source: longitude, latitude, along-strike length, downdip width, strike, dip, centroid depth, and opening. Finally, a conceptual model (Fig. 8) is created based on the calculated source parameters and geodetic measurements.

Results

Episodes of subsidence and uplift during 1992–2009

Our differential interferograms (Fig. 2) and continuous GPS measurements (Fig. 6) show that the Yellowstone caldera experienced four explicit episodes of subsidence and uplift between 1992 and 2009. During this time, no measurable

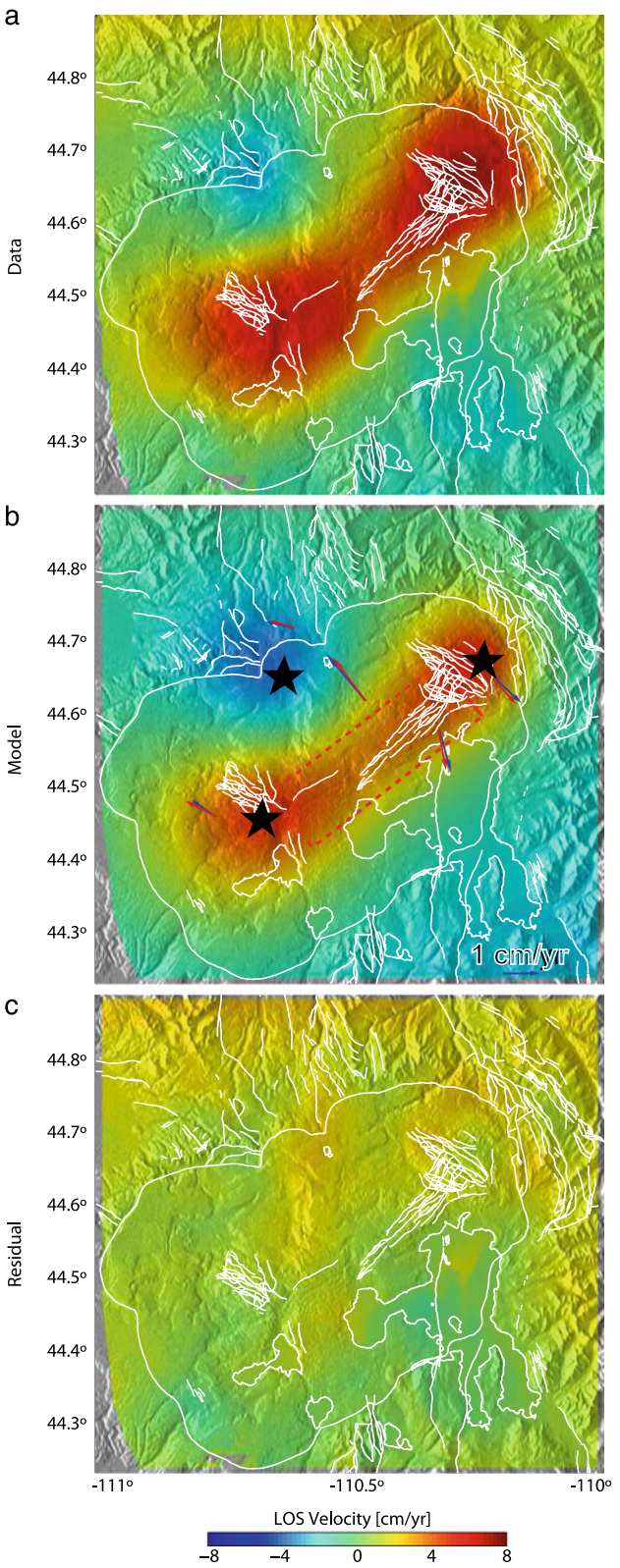

Fig. 7 The InSAR data of 2005–2006, model, and residual are represented in (**a**), (**b**), and (**c**), respectively. The *small blue arrows* in (**b**) represent the GPS data while the *small red arrows* represent the GPS model. The *red rectangle* in (**b**) is the projection of the planar source; the along-strike edge is marked with a *solid red line*. Projections of the Mogi sources are marked with *three black stars* in (**b**)

differential surface movements were recorded along the major faults within, or adjacent to, the caldera (Fig. 2). We next detail the four deformation episodes.

Episode 1: 1992–1995

During 1992–1995, broad subsidence centered on the Yellowstone caldera is observed with a maximum magnitude of ~8 cm (Fig. 2a); limited local uplift is detected near NGB (Figs. 2a and 3a). The regional-scale subsidence, marked by elongated fringes, is not restricted to the boundary of the Yellowstone caldera. During this period, the Yellowstone caldera floor subsided more rapidly, at a rate of 2.7 cm/year, than the adjacent regions that subsided at an average rate of ~0.8 cm/year (Fig. 2a).

Episode 2: 1996–2000

Uplift of ~6.8 cm is observed at the northwestern rim of the Yellowstone caldera near NGB during 1996–2000 (Figs. 2b and 3a). Slight regional subsidence by about 2 cm is measured across the caldera floor and limited deformation is detected around Hebgen Lake ~20 km west of the caldera margin. The spatial deformation pattern of uplift near NGB during 1996–2000 is distinct from the spatial deformation patterns observed during any other period in this study. Also, the magnitude of uplift is larger during the 1996–2000 period than during the previous periods of observation (Figs. 2b and 3).

Episode 3: 2000–2004

The interferogram spanning 2000–2004 shows renewed regional subsidence (~2.8 cm) across the Yellowstone caldera (Figs. 2c and 3). Measurements from the LKWY GPS station (Fig. 6a) show that this location was relatively stable between 2000 and 2001, but steady subsidence occurred between 2001 and mid-2004. However, these are point measurements and LKWY is located at the margin of Yellowstone Lake (Fig. 1), away from the center of deformation, and thus might have not detected the onset of deformation at the far-distant resurgent domes. Unfortunately, the records of WLWY and OFW2 (Fig. 6), which are located near the two resurgent domes (Fig. 1), are available only after 2004. The average rate of deformation is faster at the Sour Creek dome (~0.7 cm/year) than at the Mallard Lake dome (~0.5 cm/year; Figs. 2c, 3b, and 6a). As during the 1992–1995 period, the deformation fringes of 2000–2004 are not restricted to the Yellowstone caldera boundary, and local uplift (~2.6 cm) is observed also near NGB (Figs. 2c and 3a).

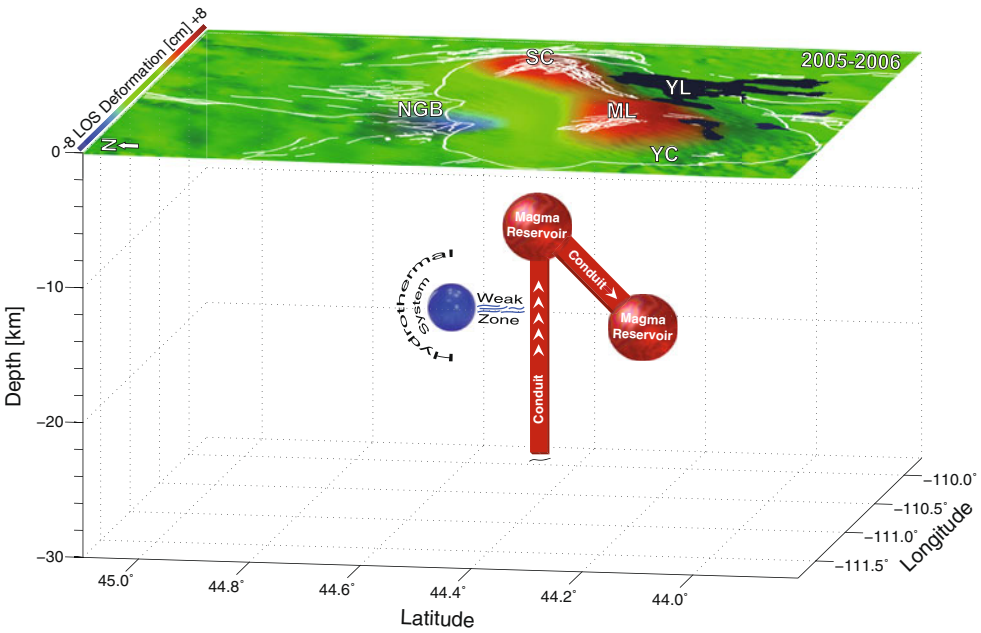

Fig. 8 Conceptual model for the Yellowstone deformation. The *white lines*, on the surface displacement map at the top of the model, represent the Quaternary faults and the *black areas* are water bodies. *YL* indicates Yellowstone Lake, *SC* Sour Creek resurgent dome, *ML* Mallard Lake resurgent dome, *YC* Yellowstone caldera, *NGB* Norris Geyser Basin

Episode 4: 2004–2009

A new episode of rapid uplift of the caldera floor began in mid-2004, as indicated by differential interferograms and continuous GPS measurements (Figs. 2d–f and 6a). We show three interferograms during this period to detail the evolution of rapid deformation across the region. The 2004–2006 interferogram shows uplift centered on the Yellowstone caldera, with deformation occurring primarily within the main caldera boundary (Figs. 2d and 6a). The Sour Creek dome experienced a higher rate of uplift (~7 cm/year) than the Mallard Lake dome (~5 cm/year). Over the same period, the central area of the caldera inflated at a rate of ~4 cm/year (Figs. 2d and 3b). These measured rates are approximately three times faster than historical inflation rates reported for Yellowstone by Pelton and Smith (1982) and Meertens and Smith (1991).

The rapid, caldera-wide, uplift was accompanied by considerable deflation (at a rate of ~4 cm/year) at the northwestern rim of the caldera near NGB (Figs. 2d, 3a, and 6a) between 2004 and 2006. The vertical motion components of WLWY, LKWY, HVWY, FOW2, and NRWY (Fig. 6a) indicate that the rapid uplift across the caldera started in mid-2004, and the deflation at NGB began in late 2004. About 1.5 cm/year of uplift also occurred around Hebgen Lake during this period (Fig. 2d). During 2004–2006, the deformation rates around NGB and Hebgen Lake increased notably compared with the detected rates in the two regions in the previous episodes.

As between 2004 and 2006, deformation during 2006–2008 was centered on the caldera but proceeded at a slower rate. Approximately 5 and 4 cm/year of uplift occurred at the Sour Creek and Mallard Lake resurgent domes, respectively (Figs. 2e, 3b, and 6a). The rate of subsidence near NGB was less than 1 cm/year, which was also significantly slower than the rate during 2004–2006. In addition, slight regional subsidence (at a rate of ~1 cm/year) occurred in the region to the north of NGB during 2006–2008 (Figs. 2e and 3a). This subsidence is aligned with the Gallatin Ridge and appears to be bordered to the east by the East Gallatin-Reese Creek (EGRC) fault zone (Fig. 1).

During 2008–2009, the rate of uplift across the Yellowstone caldera slowed to approximately 3 cm/year and subsidence virtually ceased at NGB (Figs. 2f, 3a–b, and 6a). It is notable that the deformation pattern during this period was accompanied by swarms of small earthquakes beneath Yellowstone Lake in late 2008 to early 2009, and slight regional subsidence occurred around the caldera (Figs. 2f and 3a–b).

Three-dimensional velocity field

The three-dimensional velocity field calculated for 2005–2006 indicates that the majority of observed deformation across the Yellowstone caldera and near NGB occurred in the vertical direction at rates of 6–8 and 4–5 cm/year at the two locations, respectively (Fig. 4a). Significant lateral displacements, by 5–7 cm/year in the east–west direction (Fig. 4b), occurred at the southeastern and western rims of the caldera and in the area between Hebgen Lake and NGB. Slight lateral displacements, at rates of about 0.2 cm/year in the north–south direction (Fig. 4c), also occurred in the southwestern sector of the caldera and near Yellowstone Lake.

Although the three GPS components (Fig. 6) can help in resolving the timing of deformation episodes, they lack the detailed spatial information that we can recover using

InSAR measurements. The InSAR-derived vectors for the three-dimensional velocity field of 2005–2006 match well with the three components of motion determined from GPS. The calculated ratios of the InSAR maximum horizontal displacement to the maximum vertical displacement are 0.65 and 0.75 for the Sour Creek and Mallard Lake resurgent domes, respectively.

Model source parameters

The best-fit Mogi sources for deformation at the Sour Creek and Mallard Lake resurgent domes and NGB are located at depths of 10.36, 17.27, and 16.62 km, respectively. The best-fit planar source linking the two Mogi sources beneath the resurgent domes is 10.5-km long and 33.1-km wide. It is located at depth of 13.1 km and dips by about 5° to the SW, with an opening of 0.09 m during 2005–2006. The model fits the geodetic InSAR and GPS data reasonably well with 90% confidence and the weighted and normalized root mean squares are 3.8 mm/year and 1.6, respectively. The conceptual model presented in Fig. 8 shows the modeled deformation sources with the inferred source parameters described above.

Discussion

Our differential interferograms and continuous GPS measurements during 1992–2009 imply episodic deformation across the Yellowstone caldera accompanied by deformation in an opposing direction at NGB. The observed caldera-wide subsidence of 1992–1995 might have resulted from one of two processes: (1) magma crystallization to release energy through heat of crystallization to enhance the heat flow at Yellowstone or (2) magma chamber depressurization beneath the caldera. We do not have sufficient evidence to rule out either one of these possibilities, and it is likely that both mechanisms contributed to the observed pattern of deformation. The associated uplift at Norris might have occurred due to pressurization of the Norris hydrothermal system. Dzurisin et al. (1990) and Wicks et al. (2006) reported that the widespread distribution of hydrothermal and volcanic features across the northern Yellowstone caldera boundary could indicate the presence of highly fractured and permeable crustal rocks, which might have served as pathways for migration of magmatic and hydrothermal fluids into the active caldera.

During 1996–2000, the spatial pattern and magnitude of deformation indicate a rapid rate of mass redistribution to cause a significant volume change in the magma chamber underneath the Yellowstone caldera (Vasco et al. 2007). Wicks et al. (2006) proposed migration of magmatic fluids from the caldera into NGB as a possible cause of the 1996–2000 inflation. According to Meertens et al. (2000), campaign GPS measurements between 1995 and 2000 revealed that Norris uplift began in 1995 and was followed by caldera floor subsidence between late 1997 and early 1998. During 2000–2004, the rate of uplift at Norris slowed to about 0.6 cm/year. However, the subsidence rate at the Sour Creek dome increased from 0.5 cm/year during 1996–2000 to 0.7 cm/year during 2000–2004. This probably resulted from an increased rate of crystallization or depressurization beneath the caldera, as explained above.

Between 2004 and 2009, a reversed spatial pattern of crustal deformation, with a large extent and magnitude, occurred across the entire caldera. We believe that the previous inference that inflation was caused by magma migration from NGB into the Yellowstone caldera (e.g., Wicks et al. 2006; Vasco et al. 2007) cannot be supposed for this period for two reasons. First, the small areal extent (~15×15 km) and the nature of local deflation at NGB compared to the extensive caldera-wide (60×40 km) inflation of the Yellowstone caldera are difficult to reconcile if the volume loss at NGB is to balance the volume gain in the caldera (Fig. 2d). Second, the GPS measurements show a clear delay between the onset of caldera inflation and NGB deflation. The caldera-wide uplift began in mid-2004, prior to NGB subsidence that began in late October 2004 (Fig. 6a). Therefore, direct migration of magma from NGB into the caldera is unlikely to be the mechanism responsible for inflating the entire caldera. A more likely scenario is aseismic magma injection from a deeper source beneath the Yellowstone caldera, plus magma crystallization associated with depressurization and/or fluid loss from the deep hydrothermal system beneath NGB.

The inflation of 2004–2009 started at the Sour Creek resurgent dome, which was followed by inflation (at a lower rate) at the Mallard Lake resurgent dome, as indicated by our InSAR and GPS measurements (Figs. 2d and 6a). Hence, we propose that a pulse of magma was injected from a deep mantle plume to a shallow magma reservoir beneath the Sour Creek resurgent dome through a vertical conduit. When the magma chamber reached a critical pressure, the trapped magma migrated to another shallow reservoir beneath the Mallard Lake resurgent dome via a lateral conduit (Fig. 8).

The GPS-based measurements of Meertens et al. (2000) showed that inflation was detected at NGB during the 1996–2000 episode a few months before deflation was observed across the caldera. Likewise, the caldera-wide inflation that began in mid-2004 at Yellowstone was followed a few months later by deflation at NGB (Fig. 6a). This might indicate that deflation at NGB occurred as a consequence of the Yellowstone caldera inflation. The inflation of both episodes resulted in extensive dilatational strain and likely led to an increase

in permeability, and a decrease in pore pressure, through opening fractures (Wicks et al. 2006; Chang et al. 2007). This would mean that the dilated zone around the area of inflation might have experienced lower pore pressures relative to the hydrothermal systems beneath the caldera and NGB during 1996–2000 and 2004–2009, respectively. The enhanced pressure gradient might have consequently depressurized the hydrothermal systems in both episodes, encouraging flow away from the hydrothermal systems, which might have caused the observed subsidence (or at least contributed to it partially).

The rate of deformation increased significantly near Norris and around Hebgen Lake during 2004–2006. Post-seismic viscoelastic relaxation of the M7.5 1959 Hebgen Lake earthquake was suggested previously as the main contributor to the deformation rate around Hebgen fault (e.g., Puskas et al. 2007), but such a contribution should decay over time. According to our three-dimensional velocity field, accelerated deformation of an extensional nature (in the lateral direction, S-E) occurred near Hebgen Lake during 2005–2006. This nonlinear deformation in association with the episodic crustal extensions and contractions across Yellowstone suggests that the recent surface displacements around Hebgen Lake are not likely related to the 1959 earthquake.

The deformation fringes of 1992–1995 and 2000–2004 (Fig. 2) extend beyond the Yellowstone caldera boundary. Aly et al. (2009) reported an inverse relation between the recorded deformation signals in the Yellowstone caldera and the Henrys Fork caldera during 1997–2000 and 2004–2006. They interpreted the deformation across the Henrys Fork caldera as a flexural response to magmatic processes underneath Yellowstone, or as a result of migration of hydrothermal fluids. They excluded magma migration as a possible mechanism for their observed deformation relations because magma is not expected to migrate over the lateral distance that separates the two calderas (about 30 km). However, our new interferograms that cover both calderas do not show such an inverse relation (Fig. 2). This suggests that the phenomenon reported by Aly et al. (2009) might be caused by short-term deformation, which is common in the complex Yellowstone volcanic system.

Hydrothermal convective systems are common around active magmatic centers (Aubert et al. 2005; Blatt et al. 2006; Guilbert and Park 2007). Aly et al. (2009) suggested the existence of a widespread hydrothermal convection system in the greater Yellowstone region. In this convective system, while deep groundwater is proposed to migrate toward the active caldera, shallow groundwater moves upward and away from the caldera causing regional-scale subsidence around the caldera. This explains the observed regional subsidence around the Yellowstone caldera during 2008–2009.

The seismicity record of 1992–2009 showed low-to-no spatial correlation with the InSAR observed deformation patterns (Fig. 2). The record is obtained from the University of Utah Seismographic Stations' Yellowstone National Park Earthquake Catalogs for 1983–2010. Between 1992 and 2009, seismicity was concentrated in the region between Hebgen Lake and the northwestern rim of Yellowstone caldera. This region coincides with the northern boundary of the oldest (2.05-Ma) caldera boundary and contains several north-trending young volcanic vents and active hydrothermal basins associated with the East Gallatin-Reese Creek fault zone (Puskas et al. 2007). The concentration of seismicity in this region might be related to these volcanic and hydrothermal features. Extensive seismic activity surrounding Norris occurred during 1996–2000 and showed some correlation with the deformation pattern, as shown in Fig. 2b; this seismicity might be triggered by changes in the local stress field caused by the local uplift of the region.

The association of major fissure and fault zones, such as the Elephant Back fissure and the Mirror Plateau fault zones, with the deformation patterns across the Yellowstone caldera might indicate that these structures resulted from similar episodic inflation and deflation in the past. Vasco et al. (2007) suggested that major faults in Yellowstone caldera played a significant role in controlling crustal volume increases and decreases associated with migration of volcanic and hydrothermal fluids. Our differential interferograms, however, indicate that these structures were not active during 1992–2009, as no differential movements or seismicity occurred along any fault zone during the periods of observation. Immediately adjacent to the Yellowstone caldera, we do observe regional subsidence aligned with the Gallatin Ridge and the Norris area during 2006–2008 (Fig. 2e). The observed deformation might be related to depressurization of the Norris hydrothermal system, and the EGRC fault zone might have acted as a barrier to fluids. There is no clear evidence of tectonic activity along the EGRC fault system and more data and analysis are still needed to better understand the observed pattern of deformation in this region.

Contemporary lateral extension at a rate of 5–7 cm/year across the southeastern and western rims of the Yellowstone caldera and in the area between Hebgen Lake and NGB (Fig. 4b) occurred in concert with rapid uplift across the caldera, and significant subsidence at Norris, during 2005–2006 (Fig. 4a). Savage et al. (1993) measured extension at 5.3 mm/year for a 20-km baseline across the Hebgen Lake fault between 1973 and 1987 using electronic distance measurement. Puskas et al. (2007) also reported extension across the Hebgen Lake fault with average rates varying between 3.1 mm/year (1987–1995), 5.3 mm/year (1995–2000), and 4.2 mm/year (2000–2003). The accelerated rate of lateral displacements during 2005–2006 indicated by our analysis is coincident with the caldera rapid uplift (Fig. 4a)

and, therefore, is most likely related to substantial changes in regional stress fields associated magmatic activity beneath the caldera.

Vertical displacements at the Earth's surface are very similar for various source models of different shapes if source depth is scaled appropriately (e.g., Dieterich and Decker 1975). Because the depth of deformation source is usually not known, the shape (and hence the depth) of deformation source cannot be determined based on vertical displacements alone. On the other hand, horizontal displacements are quite different for deformation sources of different shapes (Segall 2010). For this reason, we used the full three-dimensional velocity field of Fig. 4, as calculated from ascending and descending ENVISAT orbits, to constrain the shape of deformation sources beneath the Yellowstone caldera. The calculated ratios of the maximum horizontal displacement to the maximum vertical displacement for the Sour Creek and Mallard Lake resurgent domes during 2005–2006 are 0.65 and 0.75 (Fig. 5a, b). A Mogi source requires a ratio of about 0.40 between the maximum horizontal displacement and the maximum vertical displacement (e.g., Fialko et al. 2001a). The calculated values are thus consistent with two Mogi sources beneath each of the resurgent domes, as shown in Figs. 7 and 8, rather than a single sill-like body beneath the entire caldera.

Conclusions

The Yellowstone caldera experienced four discrete episodes of subsidence and uplift between 1992 and 2009. The 1992–1995 episode was characterized by regional subsidence across the caldera with local uplift near NGB. During 1996–2000, substantial uplift occurred at Norris with slight subsidence across the caldera floor. Renewed regional subsidence across the caldera, with local uplift near NGB, was recorded during 2000–2004; finally, extensive caldera-wide uplift accompanied by considerable subsidence at NGB characterized 2004–2009. Over the entire period of observation (1992–2009), no differential surface movements were detected along the major fissures and fault zones across, or adjacent to, the caldera.

We infer that magmatic and hydrothermal processes beneath the Yellowstone caldera were the main causes of deformation. Aseismic magma intrusion from a deep source beneath the Yellowstone caldera and magma crystallization, accompanied by depressurization of (and/or fluid loss from) the deep hydrothermal system beneath NGB, were the most likely causes of our observed patterns of deformation between 2004 and 2009.

The three-dimensional velocity field created from InSAR data for the 2005–2006 period implies a relation between uplift across the Yellowstone caldera floor and subsidence at NGB, with substantial lateral crustal extensions in the east–west direction at the southeastern and western rims of the caldera, as well as in the area between Hebgen Lake and NGB. Results also show lateral displacements in the north–south direction on the southwestern part of the caldera and near Yellowstone Lake.

Our models, based on the full three-dimensional deformation field calculated from InSAR measurements between 2005 and 2006, provide a new constraint on the shape of magma chamber beneath the Yellowstone caldera. The study demonstrates that a new model that considers multiple sources of deformation is an appropriate fit for the complex Yellowstone volcanic system.

Acknowledgments The ERS and ENVISAT data were provided by the European Space Agency through the GeoEarthScope Program and the Western North America Interferometric Synthetic Aperture Radar Consortium with funding from NASA, NSF, and USGS. The SRTM data were obtained from NASA JPL. The manuscript has been improved significantly with thoughtful reviews and constructive comments by James White, Andrew Harris, Lisa Morgan, and an anonymous reviewer.

References

Aly MH, Rodgers DW, Thackray GD, Hughes SS (2009) Recent magmatotectonic activity in the eastern Snake River Plain—Island Park region revealed by SAR interferometry. J Volcanol Geotherm. doi:10.1016/j.jvolgeores.2009.05.015

Aubert M, Diliberto S, Finizola A, Chébli Y (2005) Double origin of hydrothermal convective flux variations in the Fossa of Vulcano (Italy). Bull Volcanol 70(6):743–751. doi:10.1007/s00445-007-0165-y

Blatt H, Tracy RJ, Owens BE (2006) Petrology: igneous, sedimentary, and metamorphic. Macmillan, NY

Chang W, Smith RB, Wicks C, Farrell JM, Puskas, CM (2007) Accelerated uplift and magmatic intrusion of the Yellowstone Caldera, 2004 to 2006. Science 318 (952). doi:10.1126/science.1146842

Christiansen RL (2001) The Quaternary and Pliocene Yellowstone Plateau volcanic field of Wyoming, Idaho, and Montana. US Geol Surv Prof Pap 729-G

Christiansen RL, Lowenstern JB, Smith RB, Heasler H, Morgan LA, Nathenson M, Mastin LG, Muffler LJP, Robinson JE (2007) Preliminary assessment of volcanic and hydrothermal hazards in Yellowstone National Park and vicinity. U.S. Geological Survey Open-File Report 2007–1071

Dieterich JH, Decker RW (1975) Finite element modeling of surface deformation associated with volcanism. J Geophys Res 80:4094–4102

Dzurisin D, Yamashita KM (1987) Vertical surface displacements at Yellowstone caldera, Wyoming. J Geophys Res 92:753–766

Dzurisin D, Savage JC, Fournier RO (1990) Recent crustal subsidence at Yellowstone caldera, Wyoming. Bull Volcanol 52:247–270

Dzurisin D, Yamashita KM, Kleinman JW (1994) Mechanisms of crustal uplift and subsidence at the Yellowstone caldera, Wyoming. Bull Volcanol 56:261–270

Dzurisin D, Wicks C, Thatcher W (1999) Renewed uplift at the Yellowstone Caldera measured by leveling surveys and satellite radar interferometry. Bull Volcanol 61:349–355

Fialko Y (2004) Probing the mechanical properties of seismically active crust with space geodesy: study of the co-seismic deformation due to the 1992 Mw7.3 Landers (southern California) earthquake. J Geophys Res 109. doi:10.1029/2003JB002756

Fialko Y, Simons M, Khazan Y (2001a) Finite source modeling of magmatic unrest in Socorro, New Mexico, and Long Valley, California. Geophys J Int 146(1):191–200

Fialko Y, Simons M, Agnew D (2001b) The complete (3-D) surface displacement field in the epicentral area of the 1999 Mw 7.1 Hector Mine earthquake, California, from space geodetic observations. Geophys Res Lett 28(16):3063–3066

Gabriel A, Goldstein R, Zebker H (1989) Mapping small elevation changes over large areas—differential radar interferometry. J Geophys Res 94:9183–9191

Gottsmann J, Folch A, Rymer H (2006) Unrest at Campi Flegrei: a contribution to the magmatic versus hydrothermal debate from inverse and finite element modeling. J Geophys Res 111:B07203. doi:10.1029/2005JB003745

Guilbert JM, Park CE (2007) The geology of ore deposits. Waveland, Long Grove

Hoffmann J, Galloway DL, Zebker HA (2003) Inverse modeling of interbed storage parameters using land subsidence observations, Antelope Valley, California. Water Resour Res 39(2):1031. doi:10.1029/2001WR001252

Hofmann-Wellenhof B, Lichtenegger H, Collins J (1992) Global positioning system: theory and practice. Springer, NY

Hurwitz S, Christiansen LB, Hsieh PA (2007) Hydrothermal fluid flow and deformation in large calderas: influences from numerical simulations. J Geophys Res 112:B02206. doi:10.1029/2006JB004689

Massonnet D, Feigl K (1995) Discrimination of geophysical phenomena in satellite radar interferograms. Geophys Res Lett 22 (12):1537–1540

Meertens CM, Smith RB (1991) Crustal deformation of the Yellowstone caldera from first GPS measurements: 1987–1989. Geophys Res Lett 18(9):1763–1766

Meertens CM, Smith RB, Puskas CM (2000) Crustal deformation of the Yellowstone caldera from campaign and continuous GPS surveys, 1987–2000. Eos 81:V22F-19

Mogi K (1958) Relations between the eruptions of various volcanoes and the deformations of the ground surface around them. Bull Earthquake Res Inst Univ Tokyo 36:99–134

Okada Y (1985) Surface deformation due to shear and tensile faults in a halfspace. Bull Seismol Soc Am 75:1135–1154

Okada Y (1992) Internal deformation due to shear and tensile faults in a half-space. Bull Seismol Soc Am 82:1018–1040

Peltier A, Hurst T, Scott B, Cayol V (2009) Structures involved in the vertical deformation at Lake Taupo (New Zealand) between 1979 and 2007: new insights from numerical modeling. J Volcanol Geotherm 181:173–184

Pelton JR, Smith RB (1979) Recent crustal uplift in Yellowstone National Park. Science 206:1179–1182

Pelton JR, Smith RB (1982) Contemporary vertical surface displacements in Yellowstone National Park. J Geophys Res 87:2745–2761

Puskas C, Smith RB, Meertens CM, Chang WL (2007) Crustal deformation of the Yellowstone-Snake River Plain volcano-tectonic system: campaign and continuous GPS observations, 1987–2004. J Geophys Res 112:B03401. doi:10.1029/2006JB004325

Rinaldi AP, Todesco M, Bonafede M (2010) Hydrothermal instability and ground displacement at the Campi Flegrei caldera. Phys Earth Planet Inter 178:155–161

Sandwell DT, Sichoix L, Smith B (2002) The 1999 Hector Mine earthquake, Southern California: vector near-filed displacements from ERS InSAR. Bull Seismol Soc Am 92(4):1341–1354

Savage JC, Lisowski M, Prescott WH, Pitt AM (1993) Deformation from 1973 to 1987 in the epicentral area of the 1959 Hebgen Lake, Montana, earthquake (Ms=7.5). J Geophys Res 98:2145–2153

Segall P (2010) Earthquake and volcano deformation. Princeton University Press, Princeton

Simons M, Fialko Y, Rivera L (2002) Coseismic deformation from the 1999 Mw 7.1 Hector Mine, California, earthquake, as inferred from InSAR and GPS observations. Bull Seismol Soc Am 92:1390–1402

U.S. Geological Survey (2006) Quaternary fault and fold database for the United States. http//earthquakes.usgs.gov/regional/qfaults/. Cited 21 Mar 2009

Vasco DW, Puskas CM, Smith RB, Meertens CM (2007) Crustal deformation and source models of the Yellowstone volcanic field from geodetic data. J Geophys Res 112:B07402. doi:10.1029/2006JB004641

Waite GP, Smith RB (2002) Seismic evidence for fluid migration accompanying subsidence of the Yellowstone caldera. J Geophys Res 107:2177. doi:10.1029/2001JB000586

Wessel P, Smith WHF (1995) New version of the Generic Mapping Tools released. EOS Trans Am Geophys Union (76)329

Wicks C, Thatcher W, Dzurisin D (1998) Migration of fluids beneath Yellowstone Caldera inferred from satellite radar interferometry. Science 282:458–462

Wicks C, Thatcher W, Dzurisin D, Svarc J (2006) Uplift, thermal unrest, and magma intrusion at Yellowstone Caldera. Nature 440:72–75

Wright TJ, Parsons BE, Lu Z (2004) Toward mapping surface deformation in three dimensions using InSAR. Geophys Res Lett 31:L01607. doi:10.1029/2003GL018827

Yun S, Segall P, Zebker H (2005) Constraints on magma chamber geometry at Sierra Negra Volcano Galapagos Islands, based on InSAR observations. J Volcanol Geotherm. doi:10.1016/j.jvolgeores.2005.07.009

Zebker H, Rosen P, Hensley S (1997) Atmospheric effects in interferometric synthetic aperture radar surface deformation and topographic maps. J Geophys Res 102(B4):7547–7563